University Library

MINERVA ACCESS

A gateway to Melbourne's research publications

Minerva Access is the Institutional Repository of The University of Melbourne

Author/s:
Yousefpour, N;Pouragha, M

Title:
Prediction of the post-failure behavior of rocks: Combining artificial intelligence and acoustic emission sensing

Date:
2022-07-01

Citation:
Yousefpour, N. & Pouragha, M. (2022). Prediction of the post-failure behavior of rocks: Combining artificial intelligence and acoustic emission sensing. International Journal for Numerical and Analytical Methods in Geomechanics, 46 (10), pp.1874-1894. https://doi.org/10.1002/nag.3372.

Persistent Link:
https://hdl.handle.net/11343/336468

Int. J. Numer. Anal. Meth. Geomech. 0000; **00**:1–31

Published online in Wiley InterScience (www.interscience.wiley.com). DOI: 10.1002/nag

Check for updates

Prediction of the Post-Failure Behaviour of Rocks: Combining Artificial Intelligence and Acoustic Emission Sensing

Negin Yousefpour[1], Mehdi Pouragha[2*]

[1] *University of Melbourne, Dept. of Infrastructure Engineering, Parkville, Victoria, Australia*
[2] *Carleton University, Dept. of Civil and Environmental Engineering, Ottawa, Ontario, Canada*

SUMMARY

Acoustic emission (AE) reading is among the most common methods for monitoring the behaviour of brittle materials such as rock and concrete. This study uses Discrete Element Method (DEM) simulations to explore the correlations between the pre-failure AE readings with the post-failure behaviour and residual strength of rock masses. The deep learning method based on Long Short-Term Memory (LSTM) algorithms has been applied to generate predictive models based on the data from DEM simulations of biaxial compression. This dataset has been populated by varying interparticle friction while keeping bond cohesion constant. Various configurations of the LSTM algorithm were evaluated considering different scenarios for input features (strain, stress, and AE energy records) and a range of values for the key hyper-parameters. The prime AI models show promising accuracy in predicting residual strength decay with strain based on pre-failure patterns in AE readings. The results indicate that the pre-failure AE indeed encapsulates information about the developing failure mechanisms and the post-failure response in rocks, which can be captured through Artificial Intelligence. Copyright © 0000 John Wiley & Sons, Ltd.

Received ...

KEY WORDS: Acoustic emission; Rock strength; Artificial intelligence; Long short term memory (LSTM); Discrete Elements Method (DEM)

1. INTRODUCTION

Design of engineering structures supported by rock formations, such as tunnels and mines, relies heavily on accurate assessment of the strength characteristics of rock masses. The knowledge of rock mass behaviour also becomes essential in

*Correspondence to: mehdi.pouragha@carleton.ca

Copyright © 0000 John Wiley & Sons, Ltd.

Prepared using nagauth.cls *[Version: 2010/05/13 v2.00]*

This is the author manuscript accepted for publication and has undergone full peer review but has not been through the copyediting, typesetting, pagination and proofreading process, which may lead to differences between this version and the Version of Record. Please cite this article as doi: 10.1002/nag.3372

This article is protected by copyright. All rights reserved.

Author Manuscript

other fields such as reservoir engineering, seismology, and plate tectonics. Such brittle materials are prone to multiple plausible modes of failure that are affected by their complex loading history as well as the presence of heterogeneous micro-cracks and joints [1, 2].

To make matters more complex, the significant degradation in local strength following the microscopic damages makes such brittle materials prone to the so-called progressive failure mechanisms. In such cases, the seemingly random and sparse local failures quickly self-organize into global damage by continuously seeking and following the path of the least resistance [3, 4, 5, 6].

Such particularities in failure mechanisms justifiably necessitate the design processes to be complemented by appropriate ongoing monitoring systems that provide continuous feedback for reevaluating the analysis and design assumptions [7]. Given its accessibility, acoustic emission (AE) is an apt practical candidate for such a measure that can be easily recorded and tracked in situ, as well as in laboratory and numerical simulations. The acoustic energy release can well indicate processes such as crack initiation, propagation, and failure in rocks (see Figure 1). Indeed, AE sensors have been widely used in various laboratory tests and field measurements to capture the progression of rock failure (see [8] and the references therein for a complete review of the literature).

On the other hand, from the chaos theory perspective, progressive failures belong to a broad class of emergent phenomena characterized by their "sensitive dependence on initial conditions" [9, 10, 11]. From a practical point of view, such a sensitive dependence on initial sample characteristics renders the experimental investigations particularly cumbersome for two main reasons: (1) The distinct behaviour of each sample significantly hinders the systematic parametric study of the responses, and (2) the interplay between spatial correlations and material heterogeneity makes analytical interpretation of the results hard, if not impossible. For exploratory studies, such as the current one, the first issue can be partially addressed by adopting appropriate numerical simulations

Copyright © 0000 John Wiley & Sons, Ltd.

Prepared using nagauth.cls
DOI: 10.1002/nag

This article is protected by copyright. All rights reserved.

Author Manuscript

10969853, 2022, 10, Downloaded from https://onlinelibrary.wiley.com/doi/10.1002/nag.3372 by The University Of Melbourne, Wiley Online Library on [19/07/2023]. See the Terms and Conditions (https://onlinelibrary.wiley.com/terms-and-conditions) on Wiley Online Library for rules of use; OA articles are governed by the applicable Creative Commons License

as virtual experiments allowing for a systematic control over the initial and boundary conditions of the tests. The second issue, on the other hand, can be better handled by resorting to artificial intelligence (AI) algorithms that are powerful in capturing complex correlations, even if obscure to classical modeling approaches [12, 13, 14, 15].

A combination of deep learning methods with numerical simulations is particularly useful considering the non-Gaussian, non-stationary nature of the responses in rock materials, which requires a large and well-populated database. Also, systematic uncertainty quantification is required to establish robust and reliable AI models that can be eventually applied to real rock materials [16]. For such extensive studies, numerical simulations representing the real experiments can facilitate generating a comprehensive database.

Discrete Element Method (DEM) has been successfully adopted in recent years for numerical simulations of soils and rocks. The original procedure developed for granular materials was further extended in [17], where a rock medium is simulated as an assembly of tightly packed particles that are bonded to each other via cohesive interaction. The significant body of literature that followed have convincingly shown the DEM to be capable of capturing the salient mechanical aspects of rock and concrete media based on simple microscopic parameters such as interparticle contact stiffness and bond strength [18, 19, 20, 21, 22].

DEM simulations are particularly useful for the study of AE since they provide access to micro-scale data that is often not easily accessible in experiments. In particular, it is possible to track the energy release in the form of acoustic emission when a cohesive bond breaks. Recent studies have shown how DEM simulations can be used as a powerful tool to study the characteristics of AE events in rocks (and concrete) prior, during, and after failure [23, 24, 25, 26, 27].

The complex and somewhat stochastic post-failure response and its correlation with the pre-failure characteristics evade the current rock-mechanics frameworks. This is the domain where Artificial Intelligence (AI) and Machine Learning (ML),

Copyright © 0000 John Wiley & Sons, Ltd.

Prepared using nagauth.cls
DOI: 10.1002/nag

This article is protected by copyright. All rights reserved.

Author Manuscript

10969853, 2022, 10, Downloaded from https://onlinelibrary.wiley.com/doi/10.1002/nag.3372 by The University Of Melbourne, Wiley Online Library on [19/07/2023]. See the Terms and Conditions (https://onlinelibrary.wiley.com/terms-and-conditions) on Wiley Online Library for rules of use; OA articles are governed by the applicable Creative Commons License

and particularly Deep Learning (DL) methods [28] can provide powerful tools for capturing temporal correlations in AE and stress-strain data to predict the post-failure responses.

Several studies have explored ML methods, such as Artificial Neural Networks (ANNs), Support Vector Machines (SVM) and Convolutional Neural Networks (CNNs) for predicting rock strength parameters [29, 30], locating seismic events within faults [31], monitoring rock failure events in mining [32], and for crack patterns recognition in rocks [33] (see the cited references around each topic). Miah et al. [29] applied ANNs and SVMs to predict the unconfined compression strength of rocks based on field log data and identified the most relevant predictors. The developed correlations provided dynamic models for quick estimation of rock strength based on wireline logging data. Zhao et al. [31] adopted ANNs and SVM methods for relocating the hypocenters of the seismic events based on AE readings from a laboratory-scale fault. They showed that the ML methods can provide accurate assessments, as a robust alternative to complex inversion methods. Wilkins et al.[32] developed CNNs to detect, classify and locate micro-seismic events related to rock failure from sonic signals captured by geophones installed in boreholes. They demonstrated that CNNs outperform human micro-seismic expert, in recognizing both true and false events. Wang et al. [33] compared various unsupervised ML methods such as K-Means, Affinity Propagation, Mean-shift, Spectral Clustering, Ward Hierarchical Clustering, Agglomerative Clustering, Density-Based Spatial Clustering, Gaussian Mixtures, and Birch to develop a crack recognition model for rocks based on the spatial distribution of microcracks obtained from AE recordings from triaxial compression tests.

Among the most prevalent DL methods in dealing with time-series data are the Long Short-Term Memory (LSTM) networks. They belong to the broader class of Recurrent Neural Networks (RNNs) with special internal memory units that can maintain short and long temporal patterns of past time-series

Copyright © 0000 John Wiley & Sons, Ltd.

Prepared using nagauth.cls
DOI: 10.1002/nag

This article is protected by copyright. All rights reserved.

Author Manuscript

10969853, 2022, 10, Downloaded from https://onlinelibrary.wiley.com/doi/10.1002/nag.3372 by The University Of Melbourne, Wiley Online Library on [19/07/2023]. See the Terms and Conditions (https://onlinelibrary.wiley.com/terms-and-conditions) on Wiley Online Library for rules of use; OA articles are governed by the applicable Creative Commons License

data and incorporate them into future predictions [34, 35]. In addition to feed-forward connections between computational units (neurons), RNNs have recurrent connections where the output of a unit is fed back to itself with a weight and a time delay, which provides the algorithm with a memory of past activations. Stacking memory units in such networks enable learning higher levels of temporal patterns in sequential data. LSTMs have been successfully applied in a wide range of applications, such as stock market forecast, text, language, and voice recognition [36], and recently used in geotechnical engineering applications [37, 38], such as prediction of soil constitutive behaviour [39, 40], pore water pressure [41], cyclic response of granular materials [15], landslides [42], and bridge scour [43].

This paper is an exploratory study on the possibility of predicting the post-failure behaviour, in particular residual strength of rock formations, based on their pre-failure stress-strain behaviour and AE recordings using LSTMs. In particular, three fundamental questions are addressed; (1) whether or not the post-failure response of brittle materials can, in principle, be predicted from their pre-failure response; if so (2) to what extent the post-failure responses can be predicted; and (3) how deep learning methods can be used to establish such correlations. Three multivariate variants of the standard LSTM network algorithm were developed, considering more than 500 different configurations. A synthetic dataset was generated from DEM simulations of bonded particles with constant interparticle cohesion and systematically varying friction. The stress-strain and AE-strain times-series data obtained from the DEM simulations is used to develop, train and validate the LSTM models, establishing predictive relations between pre-failure AE energy variation patterns and post-failure behaviour of rock samples.

Copyright © 0000 John Wiley & Sons, Ltd.
Prepared using nagauth.cls

DOI: 10.1002/nag

This article is protected by copyright. All rights reserved.

Author Manuscript

10969853, 2022, 10, Downloaded from https://onlinelibrary.wiley.com/doi/10.1002/nag.3372 by The University Of Melbourne, Wiley Online Library on [19/07/2023]. See the Terms and Conditions (https://onlinelibrary.wiley.com/terms-and-conditions) on Wiley Online Library for rules of use; OA articles are governed by the applicable Creative Commons License

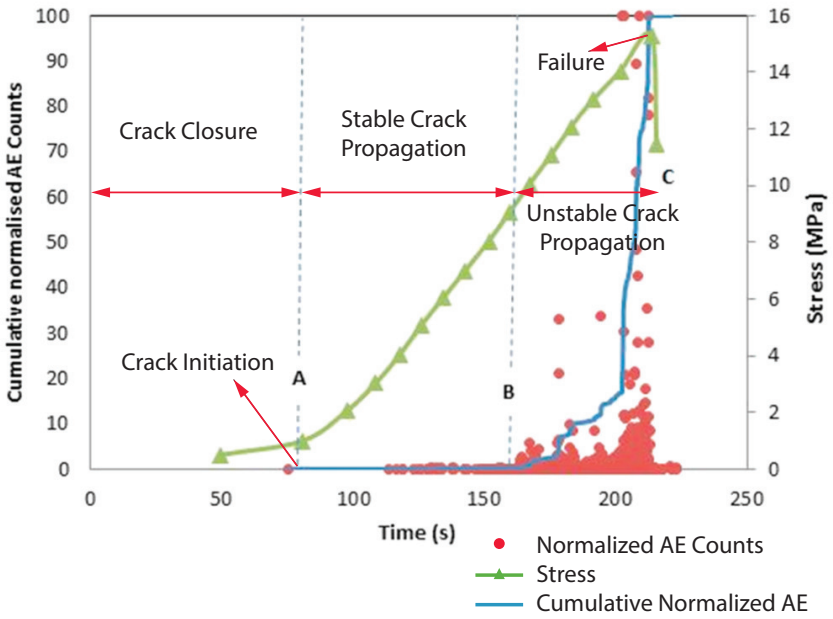

Fig. 1. A typical stress and accumulative AE counts vs strain (time), from an unconfined compression test on a Brown Coal sample [44]

2. METHODOLOGY

2.1. DEM Simulations

The open-source YADE software [45] was used to carry out two dimensional DEM simulations on assemblies of circular particles with a uniform particle size distribution between r_{min} and r_{max} with $r_{max}/r_{min} = 2.0$. The elastic contact stiffness follows a linear model with the same stiffness along the normal and tangential directions, calculated as:

$$k = E\frac{2r_1r_2}{r_1 + r_2} \tag{1}$$

where r_1 and r_2 are the radii of the two particles in contact, and E is a stiffness parameter. All samples have 1:2 aspect ratios and are confined by frictionless rigid walls. The samples were first compacted under 2D hydrostatic confinement stress of $p_0 = 5kN/m$, which, considering the average particle size of $1mm$, is equivalent to $5MPa$ in 3D. No interparticle friction or cohesion is considered in this stage to obtain a dense sample. After reaching the desired stress, the

Copyright © 0000 John Wiley & Sons, Ltd.

Prepared using nagauth.cls
DOI: 10.1002/nag

This article is protected by copyright. All rights reserved.

Author Manuscript

10969853, 2022, 10, Downloaded from https://onlinelibrary.wiley.com/doi/10.1002/nag.3372 by The University Of Melbourne, Wiley Online Library on [19/07/2023]. See the Terms and Conditions (https://onlinelibrary.wiley.com/terms-and-conditions) on Wiley Online Library for rules of use; OA articles are governed by the applicable Creative Commons License

cohesive bonds are activated at all existing contact points. The strength of these bonds are the same along with the tangential and tensile normal directions and is calculated as:

$$f_{max} = c \ \times \left(min\{r_1, r_2\} \right)^2 \tag{2}$$

where c is a stress-like parameter that controls the bond strength. After a bond is broken, a Coulomb friction law is activated restricting the tangential force with the interparticle friction coefficient of μ. In these simulations, the dimensionless initial confining pressure is $\frac{p_0}{E\,\bar{r}} = 5 \times 10^{-3}$ with $\bar{r}$ being the average particle radius, and the dimensionless bond cohesion is $\frac{c}{E} = 2.17 \times 10^{-2}$.

Given the exploratory nature of the current study, the 2D DEM simulations are not calibrated for a particular material and instead, typical parameters in the ranges commonly used in the literature are adopted here [46, 47, 48]. In turn, adopting such idealized material avoids additional complexities pertaining to the details of more realistic simulations (e.g. realistic particle shape and more elaborate contact laws) that can potentially obscure the more fundamental questions, namely, the possibility of predicting the post-failure responses based on pre-failure behavior. The answer to such basic questions can be reasonably assumed to be the same for the idealized and more realistic samples. Nevertheless, the simulations can be envisaged to be more representative of granular rock formations, such as sandstone, which are more amenable to the discrete depiction of the DEM simulations. Indeed, previous studies have demonstrated that the bonded particles picture assumed in DEM is more accurate for predicting the failure and deformation response of sandstones as compared to foliated rocks like slates [22].

The behaviour of contacts after bond breakage is governed by the interparticle friction. Therefore, the value of μ was systematically varied between 0.01 and 0.5 in different simulations to capture the effect of friction on the post-failure response. A total of 18 simulations were carried out in three series, as detailed in

Copyright © 0000 John Wiley & Sons, Ltd.
Prepared using nagauth.cls

DOI: 10.1002/nag

This article is protected by copyright. All rights reserved.

Author Manuscript

10969853, 2022, 10, Downloaded from https://onlinelibrary.wiley.com/doi/10.1002/nag.3372 by The University Of Melbourne, Wiley Online Library on [19/07/2023]. See the Terms and Conditions (https://onlinelibrary.wiley.com/terms-and-conditions) on Wiley Online Library for rules of use; OA articles are governed by the applicable Creative Commons License

Table I. DEM samples considered in this study. Each series start from a different initial particle configuration.

Test series	1	2	3
# of particles	10,000	20,000	11,000
Interparticle friction, μ	0.01, 0.02, 0.03, 0.04, 0.05, 0.06, 0.07, 0.08, 0.09, 0.10	0.05, 0.10, 0.15, 0.20, 0.30, 0.40, 0.50	0.12

Table I: 10 simulations by starting from similar initial arrangement of 10,000 particles and $\mu \in \{0.01,\ 0.02,\ 0.03,\ 0.04,\ 0.05,\ 0.06,\ 0.07,\ 0.08,\ 0.09,\ 0.10\ \}$, 7 simulations by starting from another initial arrangement of 20,000 particles and $\mu \in \{0.05,\ 0.10,\ 0.15,\ 0.20,\ 0.30,\ 0.40,\ 0.50\ \}$, and one simulation with 11,000 particles and $\mu = 0.12$. Each of the three series start from a different initial particle configuration and sample size to ensure the generality of the model and rule out the potential dependency of the subsequent AI models on initial conditions. In particular, the eventual AI models were tested based on the simulation with $11,000$ particles (series 3) whose initial configuration and friction condition differs from the rest of the simulations (series 1 and 2) adopted for training.

The biaxial quasi-static deviatoric compression loading was performed by applying a constant compressive strain rate to the top and bottom walls while the stress on the lateral walls were kept constant via a servo-control mechanism. Upon the breakage of a bond, the released elastic energy can be measured as:

$$\Delta E = \frac{f_n^2}{2\,k_n} + \frac{f_t^2}{2\,k_t} \tag{3}$$

where ΔE is the released energy due to the breakage of the bond with stiffness of k_n and k_t along the normal and tangential directions (which are the same for our simulations), and f_n and f_t are the normal and tangential components of the contact force at the time of bond breakage. The total elastic energy released was calculated by accumulating the energy of broken bonds during intervals of

Copyright © 0000 John Wiley & Sons, Ltd.

Prepared using nagauth.cls
DOI: 10.1002/nag

This article is protected by copyright. All rights reserved.

Author Manuscript

10969853, 2022, 10, Downloaded from https://onlinelibrary.wiley.com/doi/10.1002/nag.3372 by The University Of Melbourne, Wiley Online Library on [19/07/2023]. See the Terms and Conditions (https://onlinelibrary.wiley.com/terms-and-conditions) on Wiley Online Library for rules of use; OA articles are governed by the applicable Creative Commons License

the axial strain. Given the relatively narrow range of particle sizes, and hence less variation in the contact properties, the energy released during a given strain interval is found to be proportional to the number of broken bonds.

The recent results in [23] suggest that, for rock failures under tensile loading, the heterogeneity of the rock properties should be explicitly reflected in the local distribution of bond properties so as to realistically capture the distribution of AE leading to failure. The focus of this study is on compressive loading, where the results of DEM are deemed to be representative of the laboratory measurements qualitatively, if not quantitatively [49, 23].

2.2. Stress-Strain and AE Data

The variation of axial stress and AE counts (linearly scaled AE counts per unit volume, equivalent to AE energy) with axial strain is compiled in Figure 2 for various values of interparticle friction, μ. The axial stress goes through a typical brittle peak (failure stress) followed by a significant drop after which the stress is observed to fluctuate about a residual strength.

The peak and residual strengths variation with μ is compiled in Figure 3 for all the samples. Given the significant fluctuations in the post-failure response, the residual strength is calculated by time-averaging stress fluctuations within axial strain interval of $\varepsilon_{yy} = [0.025, 0.10]$. A nonlinear trend in residual (steady-state) strength is observed as the interparticle friction is increased, plateauing at a value of $\mu \simeq 0.5$, which echoes previous experimental and numerical observations [50, 51]. A rather less intuitive dependency is observed in the steady rise of the peak strength as the friction increases. While the peak strength is predominantly controlled by cohesive bond strength, our results suggest that the frictional contacts (bonds that are broken prior to the global failure) have a non-negligible contribution to the eventual global strength. Further detailed analyses of this phenomenon fall beyond the current study's scope.

Copyright © 0000 John Wiley & Sons, Ltd.

Prepared using nagauth.cls
DOI: 10.1002/nag

This article is protected by copyright. All rights reserved.

Author Manuscript

10969853, 2022, 10, Downloaded from https://onlinelibrary.wiley.com/doi/10.1002/nag.3372 by The University Of Melbourne, Wiley Online Library on [19/07/2023]. See the Terms and Conditions (https://onlinelibrary.wiley.com/terms-and-conditions) on Wiley Online Library for rules of use; OA articles are governed by the applicable Creative Commons License

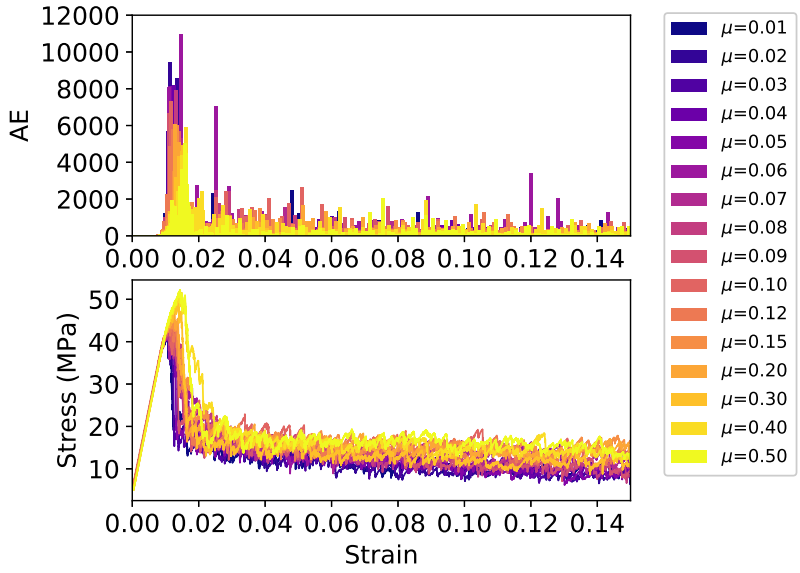

(a) Axial stress and AE vs. axial strain.

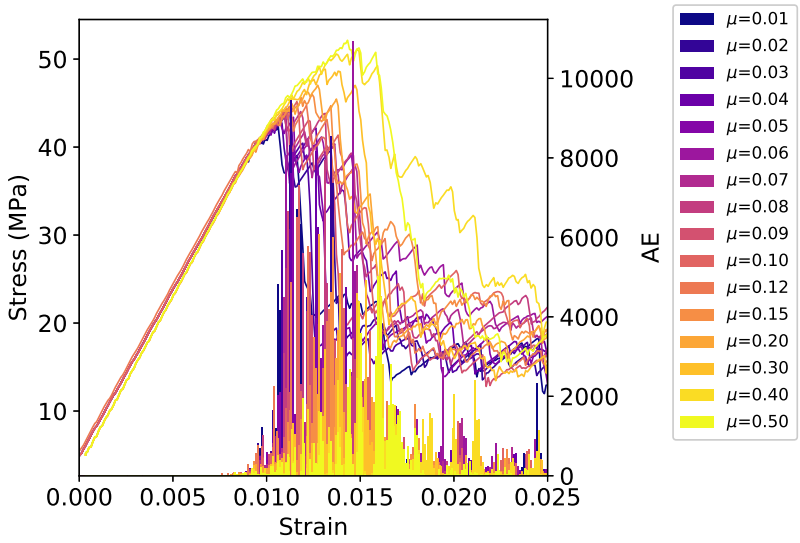

(b) Range of data used for AI training

Fig. 2. Stress-strain and AE data from DEM simulations. The results are shown for all the simulations considered in this study.

Figure 4 shows the spatial distribution of deviatoric strain, juxtaposed with the locus of AE readings, during loading of the sample with $\mu = 0.15$. At the initial stages, the damage appears as crisscrossing patterns of slip-lines diffused across the sample. However, eventually, a persisting predominant shear-band emerges that spans the sample size and leads to global failure [52]. As expected, the two fields (deviatoric strain and AE) exhibit similar patterns, confirming the

Copyright © 0000 John Wiley & Sons, Ltd.

Prepared using nagauth.cls
DOI: 10.1002/nag

This article is protected by copyright. All rights reserved.

Author Manuscript

10969853, 2022, 10, Downloaded from https://onlinelibrary.wiley.com/doi/10.1002/nag.3372 by The University Of Melbourne, Wiley Online Library on [19/07/2023]. See the Terms and Conditions (https://onlinelibrary.wiley.com/terms-and-conditions) on Wiley Online Library for rules of use; OA articles are governed by the applicable Creative Commons License

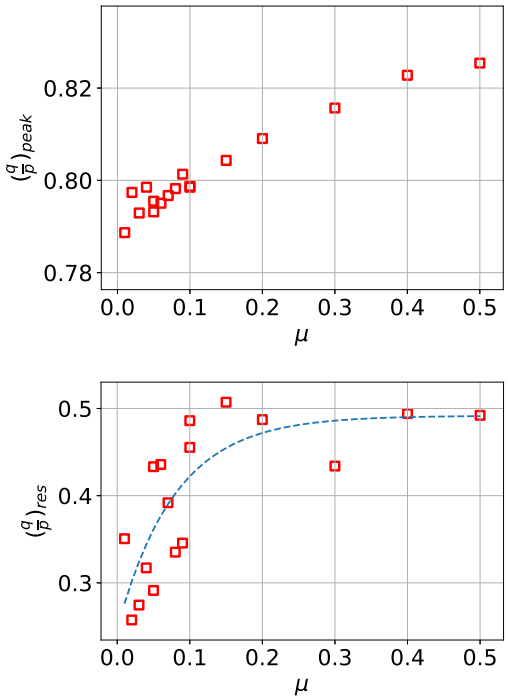

Fig. 3. Variation of deviatoric stress ratio $q/p = (\sigma_1 - \sigma_2)/(\sigma_1 + \sigma_2)$ at the peak (top) and at the residual state (bottom) with μ for all the simulated samples. The dashed line shows an exponential fit.

connection between the energy release and the developing failure mechanism [53]. The video showing the evolution of these spatial fields is provided in the supplemental materials. Similar patterns of localized failure have been widely observed and predicted in the literature [54, 55, 56, 57].

It is worth mentioning that only the results for the first 2.5% of axial strain has been used for training and validation of the AI algorithms, as the residual strength remains relatively stationary after this strain level, see Figure 2-(c).

2.3. Deep Learning using LSTMs

LSTM networks were adopted in this study to forecast the trends of post-failure stress-strain variations based on pre-failure AE data. LSTMs are known as one of the most prominent DL algorithms for learning from time-series data with the supervised approach. The LSTM memory unit overcomes the "vanishing gradients problem" that conventional deep neural networks and

Copyright © 0000 John Wiley & Sons, Ltd.

Prepared using nagauth.cls
DOI: 10.1002/nag

This article is protected by copyright. All rights reserved.

Author Manuscript

10969853, 2022, 10, Downloaded from https://onlinelibrary.wiley.com/doi/10.1002/nag.3372 by The University Of Melbourne, Wiley Online Library on [19/07/2023]. See the Terms and Conditions (https://onlinelibrary.wiley.com/terms-and-conditions) on Wiley Online Library for rules of use; OA articles are governed by the applicable Creative Commons License

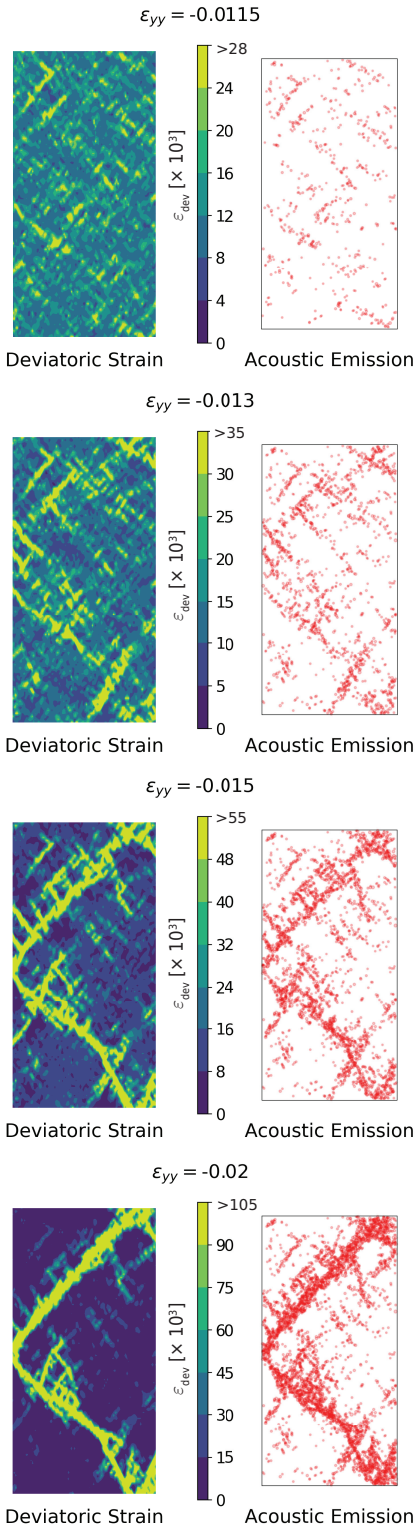

Fig. 4. Evolution of deviatoric strain and AE fields at different levels of axial strain for the sample with $\mu = 0.15$. ε_{yy} denotes the axial strain.

Copyright © 0000 John Wiley & Sons, Ltd.
Prepared using nagauth.cls

DOI: 10.1002/nag

This article is protected by copyright. All rights reserved.

Author Manuscript

10969853, 2022, 10, Downloaded from https://onlinelibrary.wiley.com/doi/10.1002/nag.3372 by The University Of Melbourne, Wiley Online Library on [19/07/2023]. See the Terms and Conditions (https://onlinelibrary.wiley.com/terms-and-conditions) on Wiley Online Library for rules of use; OA articles are governed by the applicable Creative Commons License

recurrent neural networks have, where the gradient of the weights starts to become too small or too large if the network is unfolded for too many time steps [58]. Other algorithms such as Gated Recurrent Neural Networks and Temporal Convolutional Neural Networks can also be considered as alternatives for LSTM. However, a comparative analysis of these similar algorithms lies beyond the scope of the current study [59, 60].

The key advantage of LSTMs (and DL in general) over the classical ML methods is their ability to recognize patterns and learn complex behaviors in the time-series data without a need for feature extraction. For the problem at hand, considering the complexity of rock post-failure behaviour, DL is a superior tool over the classical ML methods for recognizing the strain dependant (temporal) patterns, without a need to decompose the response into features, assuming such decomposition is feasible [61].

Figure 5 shows a diagram of the LSTM unit architecture used in this study. The algorithms were developed using TensorFlow library in Python [62]. For time-intensive computations, especially configuration optimization, codes were run on several GPUs of Spartan, the high-performance computing system at The University of Melbourne.

2.3.1. Feature Selection Three input feature combinations have been considered to evaluate and compare the performance of the AI models under various data availability scenarios. These combinations are: [strain, stress, AE], [strain, stress], and [AE], hereafter referred to as `SSAE`, `SS`, and `AE` respectively. The target feature is [stress]. The most challenging (and most practically-valuable) scenario is when the pre-failure strain-stress data is not available and the only input feature is the AE readings.

Strain was included as an input feature because the strain intervals were not constant in the DEM data. AE events were initially recorded at fine strain intervals ($\Delta\varepsilon_{yy} = 10^{-4}$) to capture the pre-failure AE trends with better

Copyright © 0000 John Wiley & Sons, Ltd.

Prepared using nagauth.cls
DOI: 10.1002/nag

This article is protected by copyright. All rights reserved.

Author Manuscript

10969853, 2022, 10, Downloaded from https://onlinelibrary.wiley.com/doi/10.1002/nag.3372 by The University Of Melbourne, Wiley Online Library on [19/07/2023]. See the Terms and Conditions (https://onlinelibrary.wiley.com/terms-and-conditions) on Wiley Online Library for rules of use; OA articles are governed by the applicable Creative Commons License

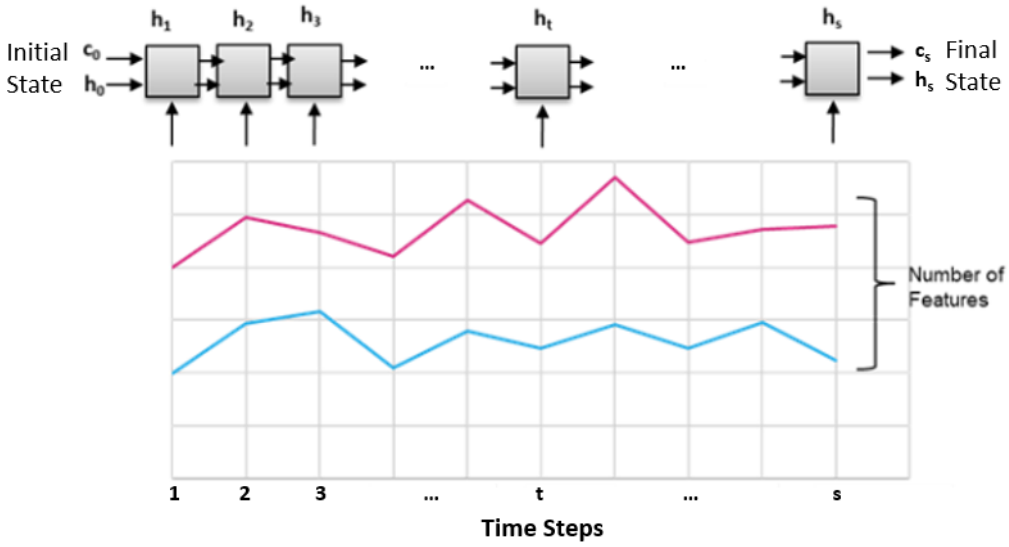

(a) LSTM unit unfolded in time

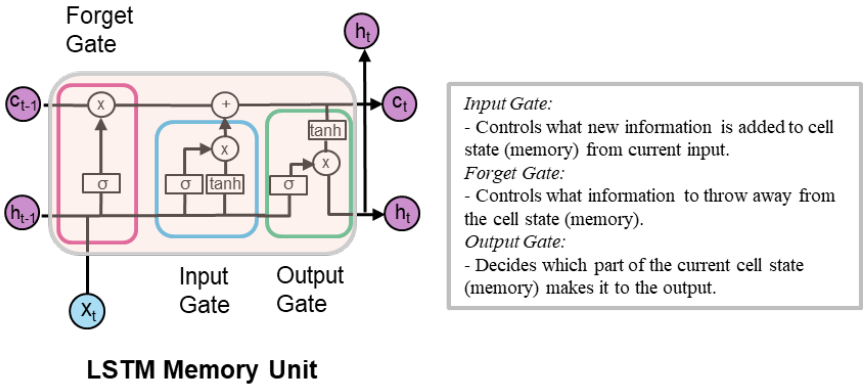

(b) LSTM memory unit and gates

Fig. 5. LSTM network architecture symbols are as follows: x_t: input, c_t: cell memory state, h_t: hidden state or output at time step t; σ: sigmoid activation function; *tanh*: hyperbolic tangent function.

accuracy. The recording interval was increased by a factor of 10 after the peak to keep the data size manageable. Variable strain intervals in AE recording occurs also in situ, where the AE rate accelerates approaching failure in rock, while the AE recordings are binned into fixed time intervals.

2.3.2. Data Partitioning Various data partitioning methods were experimented to ensure models were properly trained. For the dataset considered in this study,

Copyright © 0000 John Wiley & Sons, Ltd.
Prepared using nagauth.cls

DOI: 10.1002/nag

This article is protected by copyright. All rights reserved.

Author Manuscript

10969853, 2022, 10, Downloaded from https://onlinelibrary.wiley.com/doi/10.1002/nag.3372 by The University Of Melbourne, Wiley Online Library on [19/07/2023]. See the Terms and Conditions (https://onlinelibrary.wiley.com/terms-and-conditions) on Wiley Online Library for rules of use; OA articles are governed by the applicable Creative Commons License

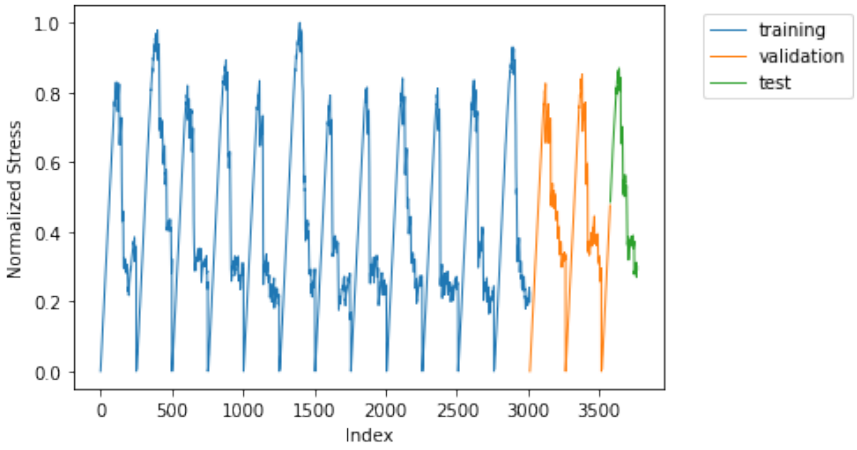

Fig. 6. Data partitioning for AI training

the division that best captured the pre-failure in training and post-failure in validation and testing was found to be 80, 15, 5% for training, testing and validation, respectively. Figure 6 shows an example of data partitioning. Note that the data has been normalized before training.

2.3.3. Training and Data Slicing To train the LSTM models, the time-series data ([strain, stress, AE]) needs to be sliced into smaller sequences using a sliding window. In each slice, a certain number of time steps are treated as inputs (input width) to the network while a number of time-steps into the future is predicted (label width). The total width for each data sequence is the sum of the input and label widths, considering no shift between input and label chains as shown in Figure 7 (offset width=label width). Figure 8 illustrates the input-label concept and data slicing scheme to generate data sequences for training the LSTMs.

The sequences in each subset of data (training, validation, and test) are divided into a number of batches. A maximum of 32 sequences are selected for each batch (batch size = 32). LSTMs were trained using the batches in the training dataset, while their performance was monitored over the batches in the validation dataset. The test dataset was used for evaluating the goodness of the model over unseen data. The LSTM performance was evaluated via the mean squared error (MSE)

Copyright © 0000 John Wiley & Sons, Ltd.
Prepared using nagauth.cls

DOI: 10.1002/nag

This article is protected by copyright. All rights reserved.

Author Manuscript

10969853, 2022, 10, Downloaded from https://onlinelibrary.wiley.com/doi/10.1002/nag.3372 by The University Of Melbourne, Wiley Online Library on [19/07/2023]. See the Terms and Conditions (https://onlinelibrary.wiley.com/terms-and-conditions) on Wiley Online Library for rules of use; OA articles are governed by the applicable Creative Commons License

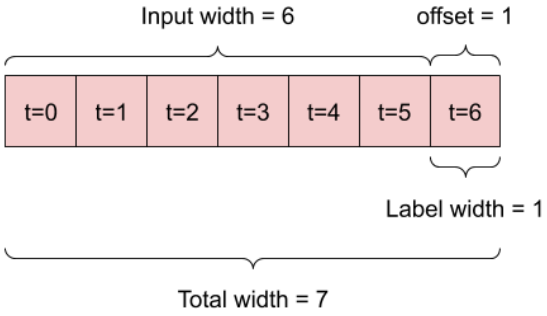

Fig. 7. Definition of input and label in data slicing; offset is the shift between inputs and labels

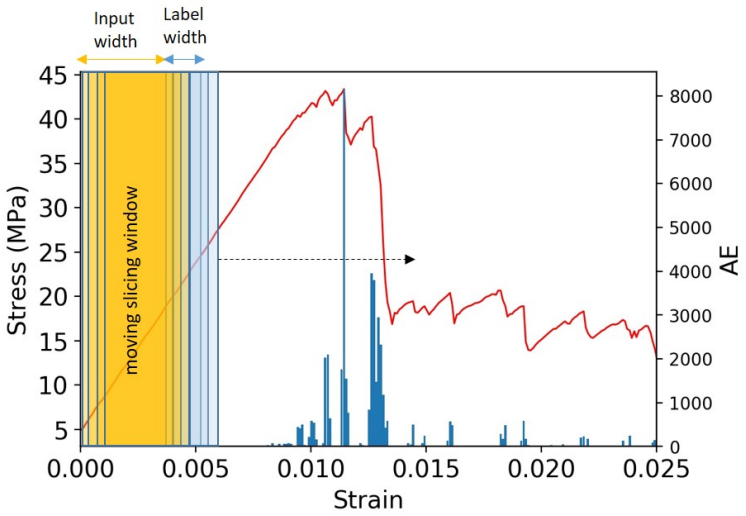

Fig. 8. Illustration of moving the slicing window over data

of predictions over the label width for all the batches in a dataset. Figure 9 provides an example of model performance during training, over the training and validation datasets. In addition to MSE, model performance was evaluated based on the mean absolute error (MAE). For each LSTM model configuration, the training process was repeated 100 times to account for randomness in the training process (initial model weights). The overall performance was evaluated based on the probabilistic distribution of the MAE values from these 100 models presented as box-plots.

Copyright © 0000 John Wiley & Sons, Ltd.

Prepared using nagauth.cls
DOI: 10.1002/nag

This article is protected by copyright. All rights reserved.

Author Manuscript

10969853, 2022, 10, Downloaded from https://onlinelibrary.wiley.com/doi/10.1002/nag.3372 by The University Of Melbourne, Wiley Online Library on [19/07/2023]. See the Terms and Conditions (https://onlinelibrary.wiley.com/terms-and-conditions) on Wiley Online Library for rules of use; OA articles are governed by the applicable Creative Commons License

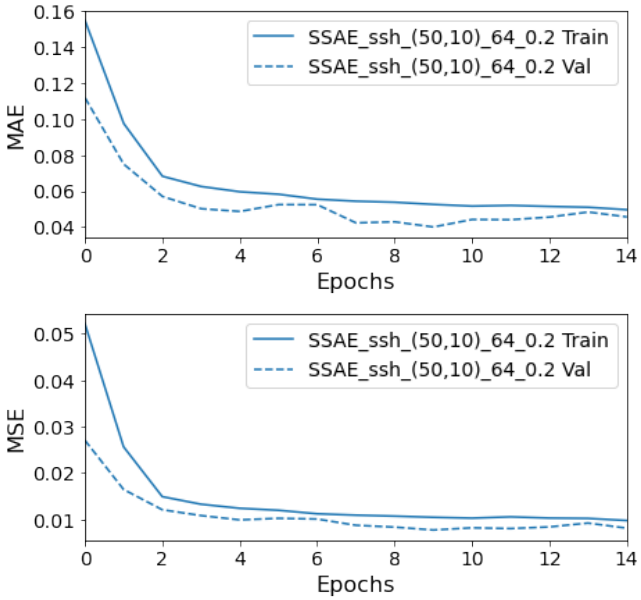

Fig. 9. Example of LSTM model performance during training

2.4. LSTM Model Variants

Three LSTM variants were developed in this study: Single-Shot (`ssh`), Feedback (`fb`) or Auto-regressive, and Single-Shot with multi LSTM layers (`ml`). The difference between Single-Shot and Feedback variants are illustrated in Figure 10.

In the single-shot method, all the label time-steps are predicted at once and the inputs to all the time steps within the label is the outputs from last time step of the input sequence. In this typical example shown, the model predicts the next 24 steps, based on the outputs of t=23. In the feedback method, the outputs from t=23 are only fed into t=24, and from there after the outputs from each time-step within the label sequence are input into the next time-step.

2.4.1. LSTM Model Configurations A grid-search was performed to find the best configurations of the LSTM models and the optimum values of the hyperparameters. The hyperparameters investigated herein are: number of LSTM layers, number of hidden units (neurons), the optimization algorithm, initial gradient decay rate, the drop-out ratio, and input-label width. The range of values tested for each hyperparameter and the selected values are given in

Copyright © 0000 John Wiley & Sons, Ltd.

Prepared using nagauth.cls
DOI: 10.1002/nag

This article is protected by copyright. All rights reserved.

Author Manuscript

10969853, 2022, 10, Downloaded from https://onlinelibrary.wiley.com/doi/10.1002/nag.3372 by The University Of Melbourne, Wiley Online Library on [19/07/2023]. See the Terms and Conditions (https://onlinelibrary.wiley.com/terms-and-conditions) on Wiley Online Library for rules of use; OA articles are governed by the applicable Creative Commons License

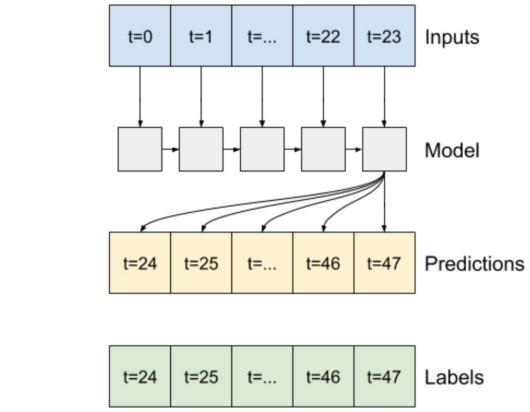

(a) single shot

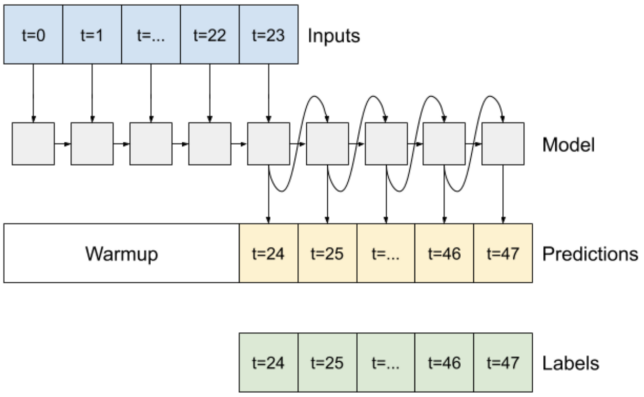

(b) feedback

Fig. 10. LSTM Variants [63].

Table II. LSTM hyper-parameters

Parameter	Tested Range	Selected Value
No. of LSTM layers	1, 2	1
No. of hidden units	32, 64, 128	64
Initial Gradient Decay Rate	0.01, 0.005, 0.001	0.005
Optimization Algorithm	SGDM, Adam and RMSProp	Adam
Dropout Ratio	0, 0.2	Variable
Input-Label Width	(20,5); (20,10); (30,10); (40,30); (50,5); (50,10); (50,20); (80,20); (80,30); (80,60); (100,50)	Variable

Table II. Based on previous studies, MSE was adopted as the loss (objective) function and the standard sigmoid was selected as the activation function for the LSTM layer [43, 64, 65].

Copyright © 0000 John Wiley & Sons, Ltd.

Prepared using nagauth.cls
DOI: 10.1002/nag

This article is protected by copyright. All rights reserved.

Author Manuscript

10969853, 2022, 10, Downloaded from https://onlinelibrary.wiley.com/doi/10.1002/nag.3372 by The University Of Melbourne, Wiley Online Library on [19/07/2023]. See the Terms and Conditions (https://onlinelibrary.wiley.com/terms-and-conditions) on Wiley Online Library for rules of use; OA articles are governed by the applicable Creative Commons License

3. RESULTS AND DISCUSSIONS

3.1. Grid Search and LSTM Configurations

The key results from grid search analyses are compiled in Figure 11 and 12, showing the box-plots of MAE of stress predictions over the test dataset for each configuration. The LSTM configuration name tags are structured as follows: `feature combination - model variant - (input width , label width) - no. of hidden units - drop-out ratio`. The feature combination, the model variant, and the input-label width showed the most significant influences on the LSTM performance, followed by the number of hidden units, the number of LSTM layers, and the drop-out ratio.

Feature combinations including strain and stress, showed much higher accuracy (smaller MAE) than those with AE being the only input feature. Comparison of MAE variation between `SSAE` and `SS` models indicates the insignificant impacts of AE when the strain-stress trend is available as an input feature. The remarkable finding here was that with the AE feature alone as an input, the AI models (with the optimal configurations) were still capable of predicting stress trends with a reasonable accuracy (MAE$\sim$ 10%). Adding other relevant input features, such as derivative (gradient) of stress and AE, could potentially further improve the performance of model. However, these are not included in the current study to avoid the "curse of dimensionality", and partly because the proposed input feature combinations showed acceptable accuracy.

Single-shot training outperformed the feedback method for most, but not all the feature combinations (compare `fb` to `ssh` in Figure 11). In particular, the feedback method resulted in larger error and variability in predictions compared to the single-shot for longer label widths [compare `(80,60)` to `(80,20)`]. Increasing the LSTM layers from one to two did not improve the performance (compare `ml` to `ssh`). Also, the optimum number of hidden neurons was found at 64 (compare `32` to `64`). Imposing a dropout of 20% during training, showed to

Copyright © 0000 John Wiley & Sons, Ltd.

Prepared using nagauth.cls
DOI: 10.1002/nag

This article is protected by copyright. All rights reserved.

Author Manuscript

10969853, 2022, 10, Downloaded from https://onlinelibrary.wiley.com/doi/10.1002/nag.3372 by The University Of Melbourne, Wiley Online Library on [19/07/2023]. See the Terms and Conditions (https://onlinelibrary.wiley.com/terms-and-conditions) on Wiley Online Library for rules of use; OA articles are governed by the applicable Creative Commons License

increase the variability in MAE, but the mean value did not show a significant improvement in accuracy (compare `0` with `0.2`).

As shown in Figure 12, for `SSAE` and `SS` models, increasing the input width from 20 to 50 resulted in a reduced accuracy for a constant label width. Increasing the input width further to 80 and then 100 showed improvement in accuracy (with a slight difference between 80 and 100). For `AE` models, increasing the input width from 20 to 50 improved the accuracy. Increasing the input width further to 80 and then 100 resulted in a significant drop in accuracy (the jump in MAE box-plots in Figure 12). In all the models, increasing the label width (while keeping the input width at constant value) consistently decreased the accuracy, i.e. the longer the prediction window, the larger the error.

Inspecting the patterns in the training data, it can be observed that AE events accelerate at an axial strain of $\sim 0.8\%$, corresponding to an index of ~ 80 (indices are the consecutive record numbers in the data matrix of strain, stress and AE counts). This explains the aforementioned performance trends with the input-label width; for cases with a slicing width (input width + label width) of less than 80, there would not be as many data sequences with non-zero AE counts. Also, for cases with a slicing width of less than 100, there would be fewer sequences covering both the pre and post failure regions of the data, as the failure consistently happens at a strain of $\sim 1\%$ (=index range of 100). Increasing the data slicing width to include more sequences covering the critical sections of the data should be balanced with the label width (prediction window length) to reach the optimum performance, as predicting too far into the future would decrease the accuracy.

3.2. AI Predictions

Examples of post-failure predictions over the test dataset ($\mu = 0.12$) for input-label of (80,60) are visualized in Figure 13 presenting the mean of predicted values (over 100 model repetitions) along with 95% confidence intervals. Also,

Copyright © 0000 John Wiley & Sons, Ltd.

Prepared using nagauth.cls
DOI: 10.1002/nag

This article is protected by copyright. All rights reserved.

Author Manuscript

10969853, 2022, 10, Downloaded from https://onlinelibrary.wiley.com/doi/10.1002/nag.3372 by The University Of Melbourne, Wiley Online Library on [19/07/2023]. See the Terms and Conditions (https://onlinelibrary.wiley.com/terms-and-conditions) on Wiley Online Library for rules of use; OA articles are governed by the applicable Creative Commons License

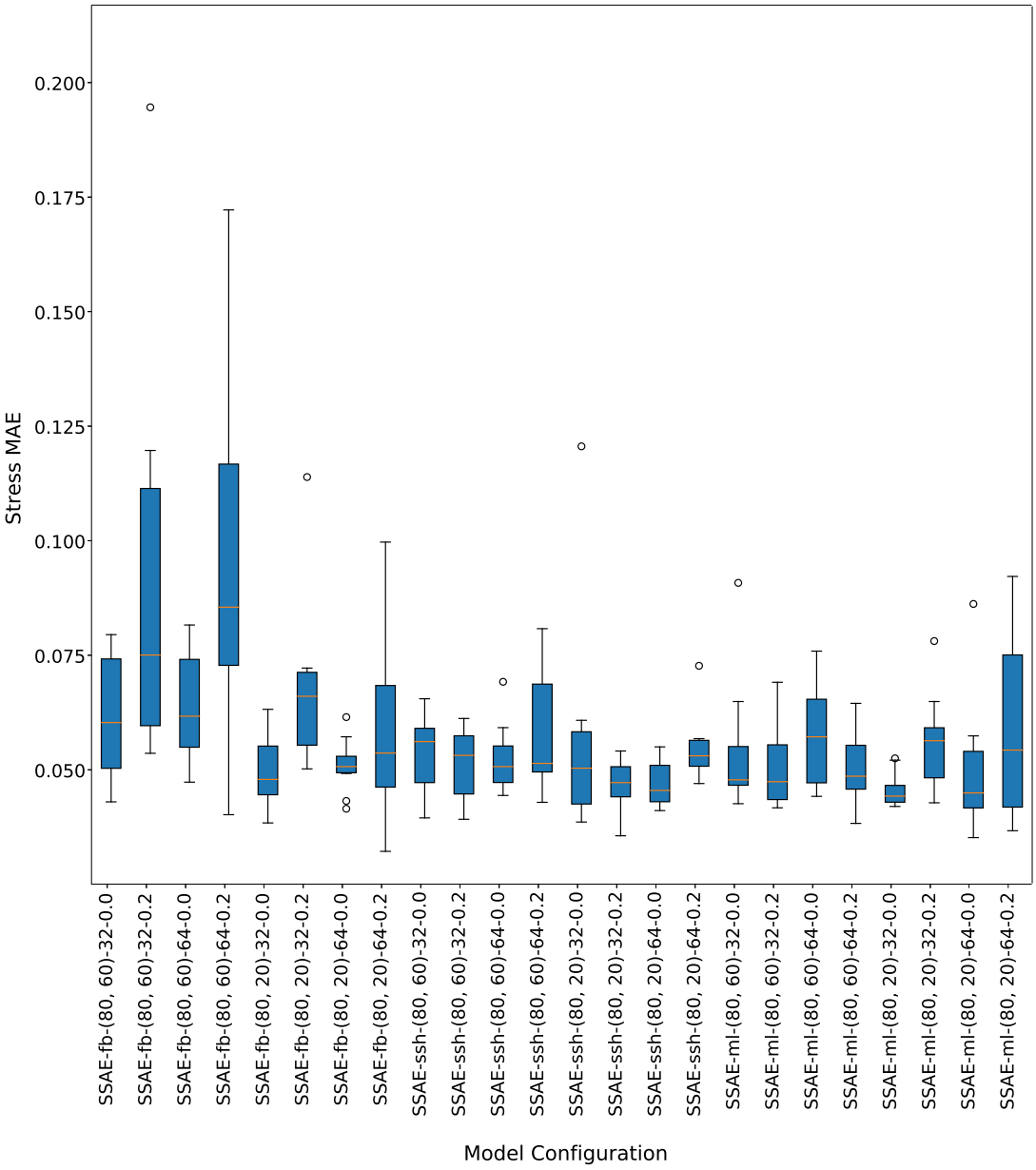

Fig. 11. Comparison of the various LSTM configurations' performance: impacts of model variant, no. of LSTM layers, no. of hidden units, and dropout ratio; the name tags are as follows: "feature combination - model variant - (input, label) - no. of hidden units - drop-out ratio".

Figures 14 to 16 show how maneuvering around input-label width can improve the performance of the AI models for each feature combination.

For `AE` (Figures 14) and input-label of (50,10), the post-failure predictions are shown to quite closely follow the actual trend of post-failure stress vs. strain. As explained in the previous section, for this feature combination, (50,10) seems to

Copyright © 0000 John Wiley & Sons, Ltd.

Prepared using nagauth.cls
DOI: 10.1002/nag

This article is protected by copyright. All rights reserved.

Author Manuscript

10969853, 2022, 10, Downloaded from https://onlinelibrary.wiley.com/doi/10.1002/nag.3372 by The University Of Melbourne, Wiley Online Library on [19/07/2023]. See the Terms and Conditions (https://onlinelibrary.wiley.com/terms-and-conditions) on Wiley Online Library for rules of use; OA articles are governed by the applicable Creative Commons License

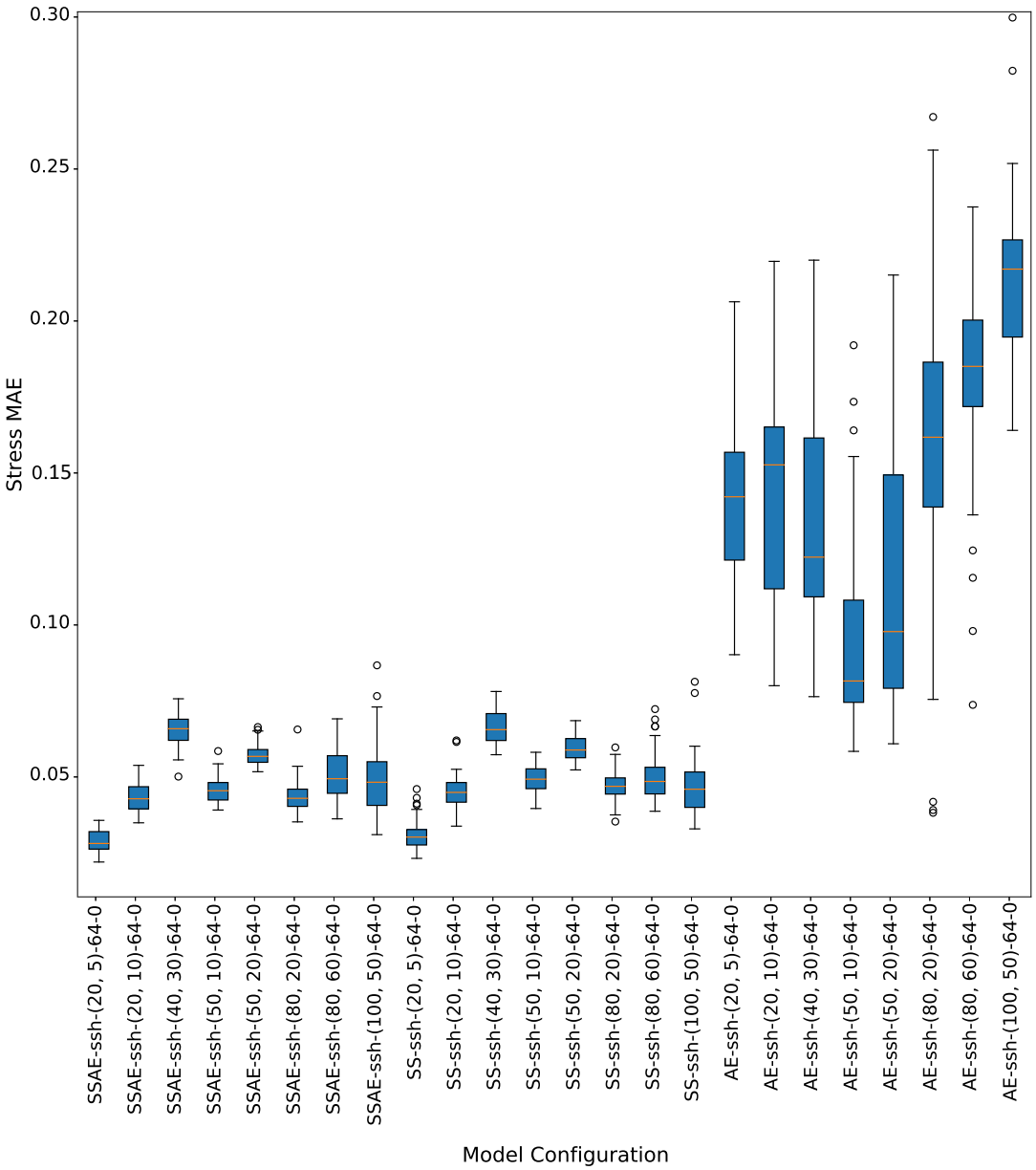

Fig. 12. Comparison of the various LSTM configurations' performance: impacts of feature combinations and input-label width

be the optimum slicing in terms of accuracy (error) and variability (uncertainty), however this comes with a compromise in the prediction window (only predicting 10 time-steps). Widening the prediction window results in less accuracy, which can be tolerable as long as the overall trend is still properly captured. The (80,60) model is a good example of this, where the post-failure prediction trends are acceptable, despite the increase in the error and variability.

Copyright © 0000 John Wiley & Sons, Ltd.

Prepared using nagauth.cls
DOI: 10.1002/nag

This article is protected by copyright. All rights reserved.

Author Manuscript

10969853, 2022, 10, Downloaded from https://onlinelibrary.wiley.com/doi/10.1002/nag.3372 by The University Of Melbourne, Wiley Online Library on [19/07/2023]. See the Terms and Conditions (https://onlinelibrary.wiley.com/terms-and-conditions) on Wiley Online Library for rules of use; OA articles are governed by the applicable Creative Commons License

For SSAE and SS (Figures 15 and Figures 16), the prediction accuracy is much higher, as discussed in the previous section, even for longer prediction windows, such as (80,60) and (100,50). However, increasing the prediction window shows a steady increase in the uncertainty.

Overall, these results show that the LSTM models with optimal configurations can capture the trends of post-failure behaviour. Most notably, the AI models with only AE as the input feature can still predict the post-failure trends with reasonable accuracy. In choosing the optimum range for slicing width (input+label width), one should take into account the frequency of the AE readings. The total slicing width should be selected considering the range of active AE recordings. Also, the prediction window should be increased gradually while observing the impacts on the trend and variability of the post-failure predictions.

4. CONCLUSIONS

This study introduces an innovative AI approach to predict the post-failure behaviour and residual strength of rocks based on the pre-failure patterns of AE energy. LSTM algorithms were successfully developed and trained using data generated through DEM simulations of rocks under compression loading. DEM simulations were performed with varying interparticle friction values and constant interparticle bond cohesion.

Various configurations (more than 500) were examined to optimize the performance of the LSTM algorithms and to find the best model set-up. Among the studied hyperparameters, the input features, model variant, and input-label width (data slicing width) were found to be the most critical. One LSTM unit with 64 hidden neurons was found as the optimal architecture. Adopting the drop-out method to avoid over-fitting during training had negligible impacts on the performance of the LSTM models. The prediction accuracy was found to be

Copyright © 0000 John Wiley & Sons, Ltd.

Prepared using nagauth.cls
DOI: 10.1002/nag

This article is protected by copyright. All rights reserved.

Author Manuscript

10969853, 2022, 10, Downloaded from https://onlinelibrary.wiley.com/doi/10.1002/nag.3372 by The University Of Melbourne, Wiley Online Library on [19/07/2023]. See the Terms and Conditions (https://onlinelibrary.wiley.com/terms-and-conditions) on Wiley Online Library for rules of use; OA articles are governed by the applicable Creative Commons License

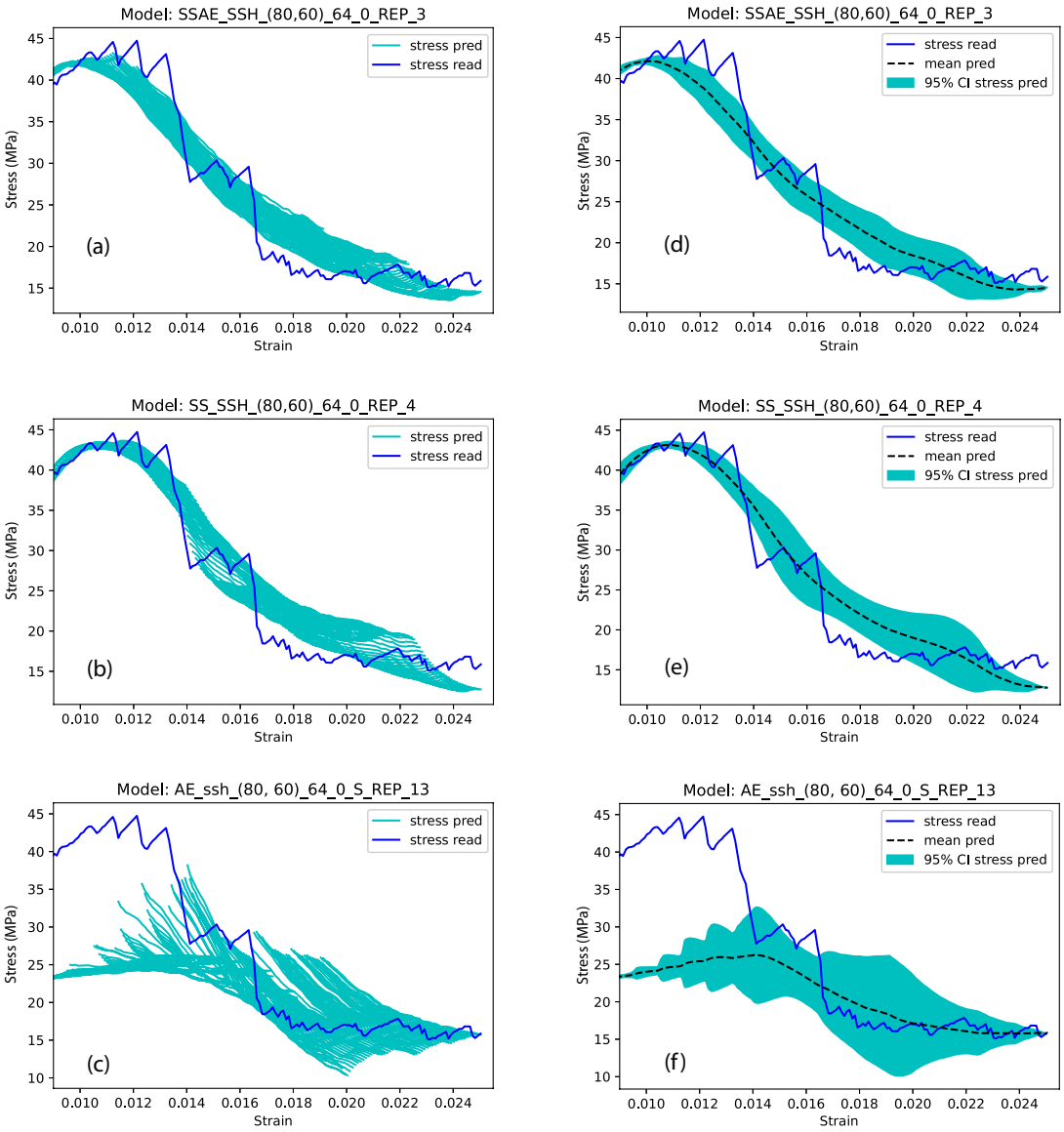

Fig. 13. Post-failure predictions by the AI models ($\mu = 0.12$): a & c) `SSAE`, b & e) `SS`, c & f) `AE`. Sub-figures a, b, and c present ensemble predictions, while d, e, and f show the 95% confidence intervals.

highly sensitive to the data slicing width and input-label width. It was shown that the best performance occurs when the slicing window results in the most informative data sequences with respect to pre and post-failure patterns of AE and stress with strain.

The optimum AI models have shown a reasonable accuracy ($< 10\%$ error) for the prediction of post-failure stress solely based on pre-failure AE data. This proves that the post-failure behaviour of brittle materials can be predicted

Copyright © 0000 John Wiley & Sons, Ltd.
Prepared using nagauth.cls

DOI: 10.1002/nag

This article is protected by copyright. All rights reserved.

Author Manuscript

10969853, 2022, 10, Downloaded from https://onlinelibrary.wiley.com/doi/10.1002/nag.3372 by The University Of Melbourne, Wiley Online Library on [19/07/2023]. See the Terms and Conditions (https://onlinelibrary.wiley.com/terms-and-conditions) on Wiley Online Library for rules of use; OA articles are governed by the applicable Creative Commons License

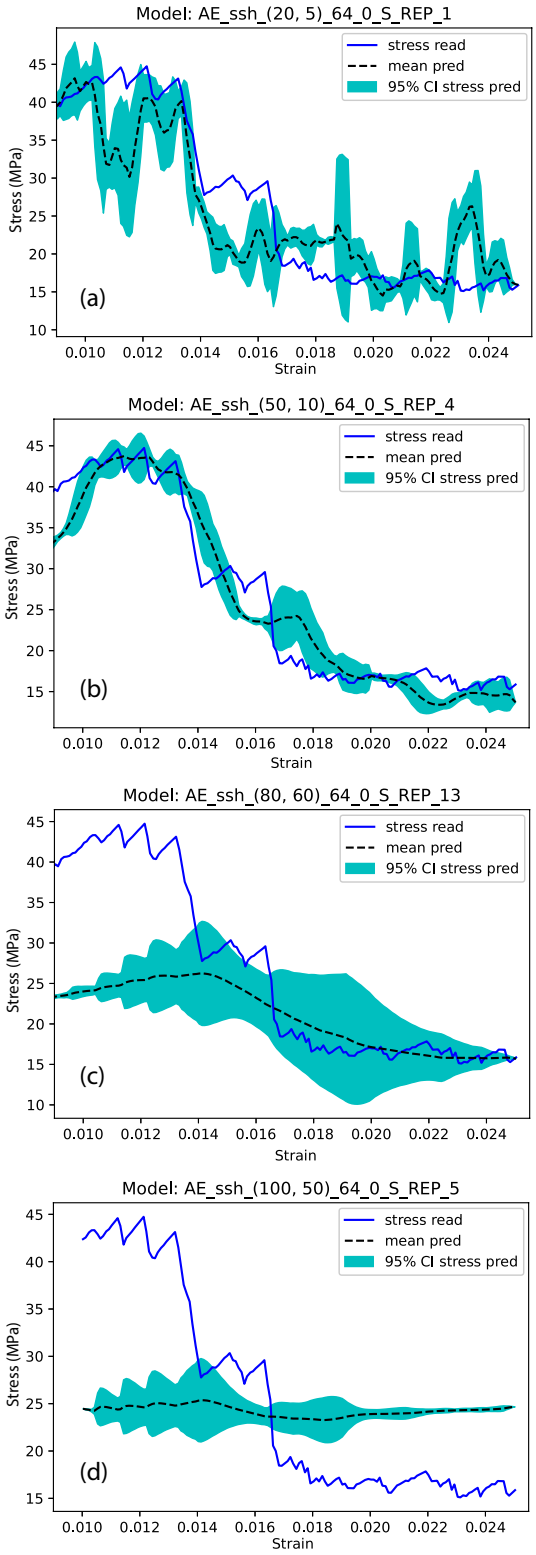

Fig. 14. Post-failure predictions for various slicing configurations for AE ($\mu = 0.12$): a)[20-5], b)[50-10], c)[80-60], d)[100-50]

Copyright © 0000 John Wiley & Sons, Ltd.
Prepared using nagauth.cls

DOI: 10.1002/nag

This article is protected by copyright. All rights reserved.

Author Manuscript

10969853, 2022, 10, Downloaded from https://onlinelibrary.wiley.com/doi/10.1002/nag.3372 by The University Of Melbourne, Wiley Online Library on [19/07/2023]. See the Terms and Conditions (https://onlinelibrary.wiley.com/terms-and-conditions) on Wiley Online Library for rules of use; OA articles are governed by the applicable Creative Commons License

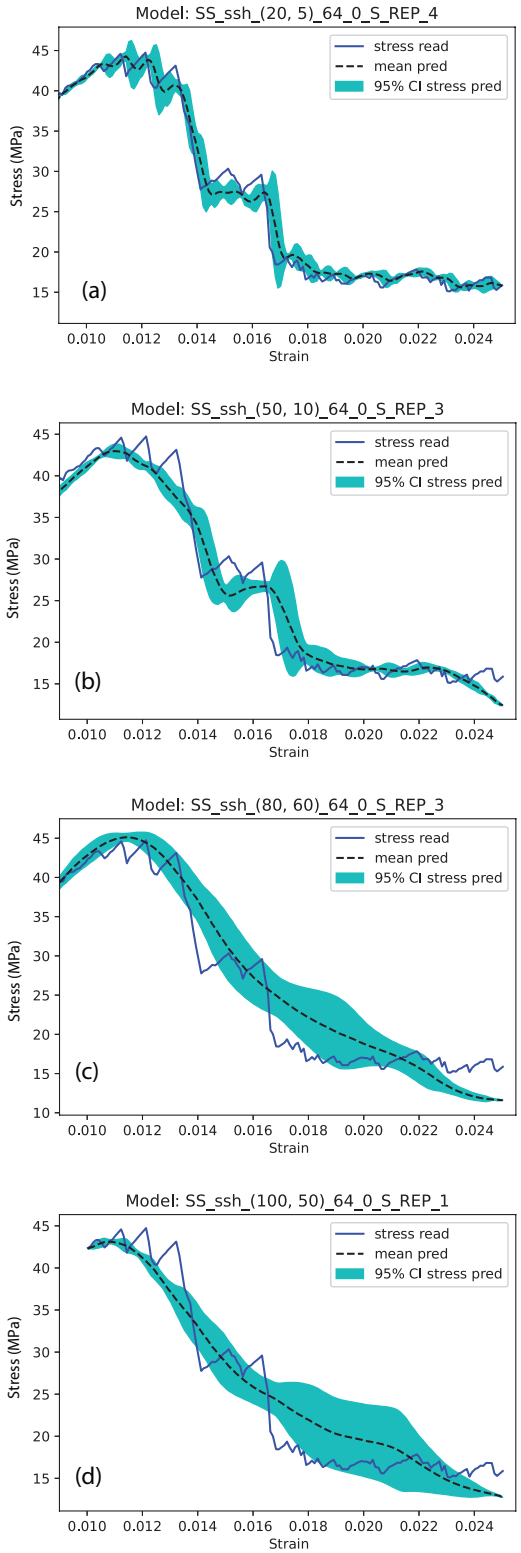

Fig. 15. Post-failure predictions for various slicing configurations for SS ($\mu = 0.12$): a)[20-5], b)[50-10], c)[80-60], d)[100-50]

Copyright © 0000 John Wiley & Sons, Ltd.
Prepared using nagauth.cls

DOI: 10.1002/nag

This article is protected by copyright. All rights reserved.

Author Manuscript

10969853, 2022, 10, Downloaded from https://onlinelibrary.wiley.com/doi/10.1002/nag.3372 by The University Of Melbourne, Wiley Online Library on [19/07/2023]. See the Terms and Conditions (https://onlinelibrary.wiley.com/terms-and-conditions) on Wiley Online Library for rules of use; OA articles are governed by the applicable Creative Commons License

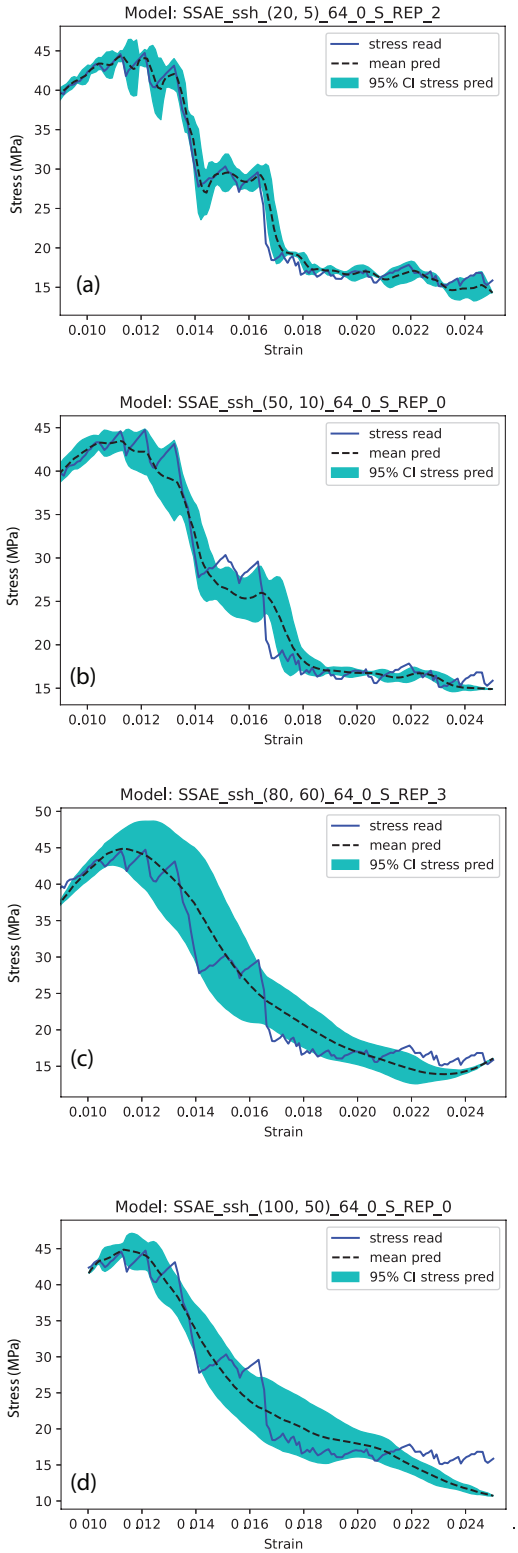

Fig. 16. Post-failure predictions for various slicing configurations for `SSAE` ($\mu = 0.12$): a)[20-5], b)[50-10], c)[80-60], d)[100-50]

Copyright © 0000 John Wiley & Sons, Ltd.
Prepared using nagauth.cls

DOI: 10.1002/nag

This article is protected by copyright. All rights reserved.

Author Manuscript

10969853, 2022, 10, Downloaded from https://onlinelibrary.wiley.com/doi/10.1002/nag.3372 by The University Of Melbourne, Wiley Online Library on [19/07/2023]. See the Terms and Conditions (https://onlinelibrary.wiley.com/terms-and-conditions) on Wiley Online Library for rules of use; OA articles are governed by the applicable Creative Commons License

from the temporal patterns of pre-failure AE events, which competent LSTM algorithms can capture.

Given the significance of the residual strength of rock masses as a design parameter, this research puts forward a novel method to provide more reliable, dynamic estimates by combining AE sensing and AI technologies. The proposed LSTM models, like any other ML model, need to be retrained with sufficient data obtained from lab or field tests (or calibrated simulations) to produce reliable predictions for a specific material. Nevertheless, it is reasonable to assume that the fundamental conclusions of the current study can still be extended to any brittle materials.

This study also reveals the remarkable potential of the deep learning methods for capturing complex patterns in the response of heterogeneous geo-materials in general. Authors hope that this proof-of-concept research paves the way for extended future investigations, incorporating real laboratory and in-situ data to upscale the proposed approach for industry applications.

ACKNOWLEDGEMENTS

This research was undertaken using the LIEF HPC-GPGPU Facility hosted at the University of Melbourne. This Facility was established with the assistance of LIEF Grant LE170100200. The financial support provided by the Natural Sciences and Engineering Research Council of Canada (RGPIN-2020-06480 and DGECR-2020-00411, held by M. Pouragha) and The University of Melbourne's Doreen Thomas Fellowship (held by Dr N. Yousefpour) is gratefully acknowledged. The authors would like to thank Dr Jordi Baró (Center of Mathematical Research, Spain) for his review and advice on the acoustic emission data.

REFERENCES

1. Lawn B. *Fracture of brittle solids*. Cambridge university press, 1993.
2. Rao Q, Sun Z, Stephansson O, Li C, Stillborg B. Shear fracture (mode ii) of brittle rock. *International Journal of Rock Mechanics and Mining Sciences* 2003; **40**(3):355–375.
3. Yang B, Xue L, Zhang K. X-ray micro-computed tomography study of the propagation of cracks in shale during uniaxial compression. *Environmental Earth Sciences* 2018; **77**(18):1–9.
4. Zhou W, Qin R, Han Kn, Wei Zy, Ma LH. Progressive damage visualization and tensile failure analysis of three-dimensional braided composites by acoustic emission and micro-ct. *Polymer Testing* 2021; **93**:106 881.
5. Mortell DJ, Tanner DA, McCarthy CT. An experimental investigation into multi-scale damage progression in laminated composites in bending. *Composite structures* 2016; **149**:33–40.

Copyright © 0000 John Wiley & Sons, Ltd.

Prepared using nagauth.cls
DOI: 10.1002/nag

This article is protected by copyright. All rights reserved.

Author Manuscript

10969853, 2022, 10, Downloaded from https://onlinelibrary.wiley.com/doi/10.1002/nag.3372 by The University Of Melbourne, Wiley Online Library on [19/07/2023]. See the Terms and Conditions (https://onlinelibrary.wiley.com/terms-and-conditions) on Wiley Online Library for rules of use; OA articles are governed by the applicable Creative Commons License

6. Prudencio M, Jan MVS. Strength and failure modes of rock mass models with non-persistent joints. *International Journal of Rock Mechanics and Mining Sciences* 2007; **44**(6):890–902.
7. Stanchits S, Burghardt J, Surdi A. Hydraulic fracturing of heterogeneous rock monitored by acoustic emission. *Rock Mechanics and Rock Engineering* 2015; **48**(6):2513–2527.
8. Feng XT, Young R, Reyes-Montes J, Aydan Ö, Ishida T, Liu JP, Liu HJ. Isrm suggested method for in situ acoustic emission monitoring of the fracturing process in rock masses. *Rock Mechanics and Rock Engineering* 2019; **52**(5):1395–1414.
9. Liao S. Chaos: A bridge from microscopic uncertainty to macroscopic randomness. *Communications in Nonlinear Science and Numerical Simulation* 2012; **17**(6):2564–2569.
10. Bai Y, Ke F, Xia M. Deterministically stochastic behavior and sensitivity to initial configuration in damage fracture. *Science Bulletin* 1994; **39**:892–895.
11. Xia M, Ke F, Wei Y, Bai J, Bai Y. Evolution induced catastrophe in a nonlinear dynamical model of material failure. *Nonlinear Dynamics* 2000; **22**(2):195–214.
12. Asghari V, Leung YF, Hsu SC. Deep neural network based framework for complex correlations in engineering metrics. *Advanced Engineering Informatics* 2020; **44**:101 058.
13. Ghaboussi J, Garrett JH, Wu X. Knowledge‐based modeling of material behavior with neural networks. *Journal of Engineering Mechanics* 1991; **117**(1):132–153, doi:10.1061/(ASCE)0733-9399(1991)117:1(132).
14. Habibagahi G, Bamdad A. A neural network framework for mechanical behavior of unsaturated soils. *Canadian Geotechnical Journal* 2003; **40**(3):684–693, doi:10.1139/t03-004. URL `https://doi.org/10.1139/t03-004`.
15. Zhang P, Yin ZY, Jin YF, Ye GL. An ai-based model for describing cyclic characteristics of granular materials. *International Journal for Numerical and Analytical Methods in Geomechanics* 2020; **44**(9):1315–1335.
16. Pouragha M, Eghbalian M, Wan R. A note on applicability of artificial intelligence to constitutive modelling of geomaterials. *Journal of Machine Learning for Modeling and Computing* 2020; **1**(2).
17. Potyondy DO, Cundall P. A bonded-particle model for rock. *International journal of rock mechanics and mining sciences* 2004; **41**(8):1329–1364.
18. Jing L, Stephansson O. *Fundamentals of discrete element methods for rock engineering: theory and applications*, vol. 85. Elsevier, 2007.
19. Rojek J, Onate E, Labra C, Kargl H. Discrete element simulation of rock cutting. *International Journal of Rock Mechanics and Mining Sciences* 2011; **48**(6):996–1010.
20. Scholtès L, Donzé FV. Modelling progressive failure in fractured rock masses using a 3d discrete element method. *International Journal of Rock Mechanics and Mining Sciences* 2012; **52**:18–30.
21. Duriez J, Darve F, Donze FV. A discrete modeling-based constitutive relation for infilled rock joints. *International journal of rock mechanics and mining sciences* 2011; **48**(3):458–468.
22. Pouragha M, Eghbalian M, Wan R. Micromechanical correlation between elasticity and strength characteristics of anisotropic rocks. *International Journal of Rock Mechanics and Mining Sciences* 2020; **125**:104 154.
23. Caulk RA. Modeling acoustic emissions in heterogeneous rocks during tensile fracture with the discrete element method. *Open Geomechanics* 2020; **2**.
24. Xie C, Yuan L, Zhao M, Jia Y. Study on failure mechanism of porous concrete based on acoustic emission and discrete element method. *Construction and Building Materials* 2020; **235**:117 409.
25. Gao K, Guyer R, Rougier E, Ren CX, Johnson PA. From stress chains to acoustic emission. *Physical review letters* 2019; **123**(4):048 003.
26. Ma J, Wu S, Zhang XP, Gan Y. Modeling acoustic emission in the brazilian test using moment tensor inversion. *Computers and Geotechnics* 2020; **123**:103 567.
27. Wang Z, Wang T, Wu S, Hao Y. Investigation of microcracking behaviors in brittle rock using polygonal grain-based distinct method. *International Journal for Numerical and Analytical Methods in Geomechanics* 2021; .
28. Deng L, Yu D. Deep learning: Methods and applications. *Technical Report*, Microsoft May 2014.
29. Miah MI, Ahmed S, Zendehboudi S, Butt S. Machine learning approach to model rock strength: Prediction and variable selection with aid of log data. *Rock Mechanics and Rock Engineering* 2020; **53**(10):4691–4715.
30. Ceryan N, Okkan U, Samui P, Ceryan S. Modeling of tensile strength of rocks materials based on support vector machines approaches. *International Journal for Numerical and Analytical Methods in Geomechanics* 2013; **37**(16):2655–2670.

Copyright © 0000 John Wiley & Sons, Ltd.
Prepared using nagauth.cls

DOI: 10.1002/nag

This article is protected by copyright. All rights reserved.

Author Manuscript

10969853, 2022, 10, Downloaded from https://onlinelibrary.wiley.com/doi/10.1002/nag.3372 by The University Of Melbourne, Wiley Online Library on [19/07/2023]. See the Terms and Conditions (https://onlinelibrary.wiley.com/terms-and-conditions) on Wiley Online Library for rules of use; OA articles are governed by the applicable Creative Commons License

31. Zhao Q, Glaser SD. Relocating acoustic emission in rocks with unknown velocity structure with machine learning. *Rock Mechanics and Rock Engineering* 2020; **53**(5):2053–2061.
32. Wilkins AH, Strange A, Duan Y, Luo X. Identifying microseismic events in a mining scenario using a convolutional neural network. *Computers & Geosciences* 2020; **137**:104 418, doi:https://doi.org/10.1016/j.cageo.2020.104418. URL `https://www.sciencedirect.com/science/article/pii/S0098300419307174`.
33. Wang C, Hou X, Liu Y. Three-dimensional crack recognition by unsupervised machine learning. *Rock Mechanics and Rock Engineering* 2021; **54**(2):893–903.
34. Hochreiter S, Schmidhuber J. Long short-term memory. *Neural computation* 1997; **9**(8):1735–1780.
35. Ordóñez FJ, Roggen D. Deep convolutional and lstm recurrent neural networks for multimodal wearable activity recognition. *Sensors* 2016; **16**(1):115.
36. Ray A, Rajeswar S, Chaudhury S. Text recognition using deep blstm networks. *2015 Eighth International Conference on Advances in Pattern Recognition (ICAPR)*, 2015; 1–6, doi:10.1109/ICAPR.2015.7050699.
37. Zhang W, Li H, Li Y, Liu H, Chen Y, Ding X. Application of deep learning algorithms in geotechnical engineering: a short critical review. *Artificial Intelligence Review* 2021; :1–41.
38. Zhang J, Wang Y, Sun Y, Li G. Strength of ensemble learning in multiclass classification of rockburst intensity. *International Journal for Numerical and Analytical Methods in Geomechanics* 2020; **44**(13):1833–1853.
39. Zhang P, Yin ZY, Jin YF, Ye GL. An ai-based model for describing cyclic characteristics of granular materials. *International Journal for Numerical and Analytical Methods in Geomechanics* ; **44**(9):1315–1335, doi:https://doi.org/10.1002/nag.3063. URL `https://onlinelibrary.wiley.com/doi/abs/10.1002/nag.3063`.
40. Zhang N, Shen SL, Zhou A, Jin YF. Application of lstm approach for modelling stress–strain behaviour of soil. *Applied Soft Computing* 2021; **100**:106 959, doi:https://doi.org/10.1016/j.asoc.2020.106959. URL `https://www.sciencedirect.com/science/article/pii/S1568494620308978`.
41. Wei X, Zhang L, Yang HQ, Zhang L, Yao YP. Machine learning for pore-water pressure time-series prediction: Application of recurrent neural networks. *Geoscience Frontiers* 2021; **12**(1):453–467, doi:https://doi.org/10.1016/j.gsf.2020.04.011. URL `https://www.sciencedirect.com/science/article/pii/S1674987120301134`.
42. Xie P, Zhou A, Chai B. The application of long short-term memory(lstm) method on displacement prediction of multifactor-induced landslides. *IEEE Access* 2019; **7**:54 305–54 311, doi:10.1109/ACCESS.2019.2912419.
43. Yousefpour N, Downie S, Walker S, Perkins N, Dikanski H. Machine learning solutions for bridge scour forecast based on monitoring data. *Transportation Research Record* 2021; :03611981211012 693.
44. Vishal V, Ranjith P, Singh T. 2015; **22**:428–436, doi:https://doi.org/10.1016/j.jngse.2014.12.020. URL `https://www.sciencedirect.com/science/article/pii/S1875510014003989`.
45. Šmilauer V, Catalano E, Chareyre B, Dorofeenko S, Duriez J, Gladky A, Kozicki J, Modenese C, Scholtès L, Sibille L, *et al.*. Yade reference documentation. *Yade Documentation* 2010; **474**:1–531.
46. Froiio F, Roux JN. Incremental response of a model granular material by stress probing with dem simulations. *AIP Conference Proceedings*, vol. 1227, American Institute of Physics, 2010; 183–197.
47. Nitka M, Combe G, Dascalu C, Desrues J. Two-scale modeling of granular materials: a dem-fem approach. *Granular Matter* 2011; **13**(3):277–281.
48. Nguyen NH, Bui HH, Nguyen GD, Kodikara J. A cohesive damage-plasticity model for dem and its application for numerical investigation of soft rock fracture properties. *International Journal of Plasticity* 2017; **98**:175–196.
49. Hazzard J, Young RP. Dynamic modelling of induced seismicity. *International journal of rock mechanics and mining sciences* 2004; **41**(8):1365–1376.
50. Härtl J, Ooi JY. Experiments and simulations of direct shear tests: porosity, contact friction and bulk friction. *Granular Matter* 2008; **10**(4):263.
51. Radjai F, Azéma E. Shear strength of granular materials. *European journal of environmental and civil engineering* 2009; **13**(2):203–218.
52. Zhou S, Tordesillas A, Pouragha M, Bailey J, Bondell H. On local intrinsic dimensionality of deformation in complex materials. *Scientific reports* 2021; **11**(1):1–14.
53. Baró J, Pouragha M, Wan R, Davidsen J. Quasistatic kinetic avalanches and self-organized criticality in deviatorically loaded granular media. *Physical Review E* 2021; **104**(2):024 901.

Copyright © 0000 John Wiley & Sons, Ltd.

Prepared using nagauth.cls
DOI: 10.1002/nag

This article is protected by copyright. All rights reserved.

Author Manuscript

10969853, 2022, 10, Downloaded from https://onlinelibrary.wiley.com/doi/10.1002/nag.3372 by The University Of Melbourne, Wiley Online Library on [19/07/2023]. See the Terms and Conditions (https://onlinelibrary.wiley.com/terms-and-conditions) on Wiley Online Library for rules of use; OA articles are governed by the applicable Creative Commons License

54. Darve F, Nicot F, Wautier A, Liu J. Slip lines versus shear bands: two competing localization modes. *Mechanics Research Communications* 2021; **114**:103 603.
55. Amirrahmat S, Alshibli KA, Jarrar MF, Zhang B, Regueiro RA. Equivalent continuum strain calculations based on 3d particle kinematic measurements of sand. *International Journal for Numerical and Analytical Methods in Geomechanics* 2018; **42**(8):999–1015.
56. Amirrahmat S, Druckrey AM, Alshibli KA, Al-Raoush RI. Micro shear bands: Precursor for strain localization in sheared granular materials. *Journal of Geotechnical and Geoenvironmental Engineering* 2019; **145**(2):04018 104.
57. Nguyen GD, Einav I, Korsunsky AM. How to connect two scales of behaviour in constitutive modelling of geomaterials. *Géotechnique Letters* 2012; **2**(3):129–134.
58. Bengio Y, Simard P, Frasconi P. Learning long-term dependencies with gradient descent is difficult. *IEEE transactions on neural networks* 1994; **5**(2):157–166.
59. Almqvist O. A comparative study between algorithms for time series forecasting on customer prediction: An investigation into the performance of arima, rnn, lstm, tcn and hmm, phd thesis 06 2019.
60. Chung J, Gulcehre C, Cho K, Bengio Y. Empirical evaluation of gated recurrent neural networks on sequence modeling. arxiv 2014. *arXiv preprint arXiv:1412.3555* 2014; .
61. Chauhan NK, Singh K. A review on conventional machine learning vs deep learning. *2018 International conference on computing, power and communication technologies (GUCON)*, IEEE, 2018; 347–352.
62. Abadi M, Agarwal A, Barham P, Brevdo E, Chen Z, Citro C, Corrado GS, Davis A, Dean J, Devin M, *et al.*. TensorFlow: Large-scale machine learning on heterogeneous systems 2015. URL `https://www.tensorflow.org/`, software available from tensorflow.org.
63. Google. Time series forecasting.
64. Greff K, Srivastava RK, Koutník J, Steunebrink BR, Schmidhuber J. LSTM: A search space odyssey. *CoRR* 2015; **abs/1503.04069**.
65. Elsworth S, Güttel S. Time series forecasting using LSTM networks: A symbolic approach. *CoRR* 2020; **abs/2003.05672**.

Copyright © 0000 John Wiley & Sons, Ltd.
Prepared using nagauth.cls

DOI: 10.1002/nag

This article is protected by copyright. All rights reserved.

Author Manuscript

10969853, 2022, 10, Downloaded from https://onlinelibrary.wiley.com/doi/10.1002/nag.3372 by The University Of Melbourne, Wiley Online Library on [19/07/2023]. See the Terms and Conditions (https://onlinelibrary.wiley.com/terms-and-conditions) on Wiley Online Library for rules of use; OA articles are governed by the applicable Creative Commons License